







## Pushing magnetic spirals beyond room temperature by reducing the uniaxial pyramidal elongation in layered Cu/Fe perovskites

Xiaodong Zhang <sup>1</sup>, Arnau Romaguera <sup>1</sup>, Oscar Fabelo <sup>2</sup>, Francois Fauth <sup>3</sup>,  
Javier Herrero-Martin <sup>3</sup> and José Luis García-Muñoz <sup>1,\*</sup>

<sup>1</sup>*Institut de Ciència de Materials de Barcelona, ICMAB-CSIC, Campus UAB, 08193 Bellaterra, Spain*

<sup>2</sup>*Institut Laue-Langevin, 71 avenue des Martyrs, 38042 Grenoble, France*

<sup>3</sup>*ALBA Synchrotron Light Source, 08290 Cerdanyola del Vallès, Barcelona, Spain*



(Received 8 December 2023; accepted 5 June 2024; published 17 July 2024)

The impact of a 3d divalent substitution for Cu using  $M^{2+}$  ions not presenting elongated  $MO_5$  pyramids has been explored in  $YBaCuFeO_5$  as a new strategy to upgrade the magnetic properties of this high-temperature spiral magnet and potential multiferroic. In this work we investigate the incidence of the  $Cu^{2+}$  with  $Co^{2+}$  substitution in  $YBa(Cu_{1-x}Co_x)FeO_5$  compounds in which B-site disorder is kept invariant (disorder  $n_d \approx 36\%$ ). The study validates the reduction of the uniaxial elongation distortion at Cu sites as an efficient alternative way to disorder that enables one to enhance the thermal stability of the spiral order. In addition, the rotation plane of the helix is reoriented by the Cu/Co substitution and nearby the triple point (when  $T_S$  is maximal) the spiral order adopts an almost complete cycloidal magnetic configuration. These results lay the foundation of a new mechanism to tune the stability of the magnetic spirals in layered perovskites based on reducing the uniaxial elongation associated to the (4+1)-coordination of  $Cu^{2+}$  ions in square  $CuO_5$  pyramids.

DOI: [10.1103/PhysRevResearch.6.033081](https://doi.org/10.1103/PhysRevResearch.6.033081)

### I. INTRODUCTION

The materials presenting chiral magnetic structures are attracting a lot of attention. They form a rare subclass within the class of magnetically frustrated compounds where all mirror symmetries are broken: their mirror images cannot be recovered by any combination of spatial rotations and translations. Moreover, time-reversal symmetry operations necessarily preserve a steady chiral state: a left-type state cannot be transformed into a right- one under time-reversal symmetry operations [1].

Among the properties favored by chiral magnetic orders, the multiferroicity is a very attractive one. In contrast to other types of multiferroics with weak magnetoelectric coupling, the spin and ferroelectric orders are intrinsically coupled in multiferroics induced by cycloidal orders, which favors higher magnetoelectric responses. In most of the latter, the spin-orbit coupling induces ferroelectric polarization in the spiral phase through the Dzyaloshinskii-Moriya (DM) interaction. Nevertheless, an issue is that magnetic frustration strongly restricts the spiral magnetic orders below (typically)  $T_S < 50$  K [2,3]. Rare exceptions of high- $T_S$  spiral multiferroics are some hexaferrites and CuO. Some longitudinal conical hexaferrites (e.g.,  $Ba_{0.8}Sr_{1.2}Co_2Fe_{12-x}Al_xO_{22}$ ) can adopt a transverse ferroelectric state at room temperature when a magnetic field

is applied off the screw axis, although higher values of the linear magnetoelectric effect are required for practical devices [4,5]. CuO is a rare known example of high-temperature spiral multiferroic (at zero magnetic field and temperatures above 200 K) [6]. But its spiral phase is stable only within the narrow interval 213–230 K due to the balance between the easy plane anisotropy and exchange interaction energies. Moreover, the multiferroic phase in CuO reaches 295 K with the application of 18.5 GPa pressure [7].

The layered perovskites  $RBaCuFeO_5$  ( $R$ : rare-earth or Y) are a rare exception because spiral magnetic order ( $T_S$ ) has been reported at much higher temperatures ( $T_S > 200$  K) and even beyond RT. Several reports disclosing electric polarization associated to the spiral phase of some of these perovskites [8,9] have raised much expectation as promising candidates to high- $T_S$  spin-driven multiferroics for low-power magnetoelectric applications [10,11].

While cations at the A site of the  $YBaCuFeO_5$  perovskite ( $Y^{3+}$ ,  $Ba^{2+}$ ) order in alternating layers perpendicular to the  $c$  axis, the spatial distribution of  $Cu^{2+}O_5$  and  $Fe^{3+}O_5$  pyramids exhibits different degree of disorder depending on the preparation method [10,12]. The importance of the Cu/Fe disorder is linked to its impact on the magnetic interactions because their sign or strength change depending on the spatial distribution of  $Fe^{3+}$  and  $Cu^{2+}$  ions. Parallel to the  $c$  axis, the Cu-O-Fe exchange ( $J_{c2}$ ) within  $Cu^{2+}Fe^{3+}O_9$  bipyramids is the only ferromagnetic [9]. Its sign changes in the bipyramids of the type  $Fe^{3+}Fe^{3+}O_9$  or  $Cu^{2+}Cu^{2+}O_9$ , generating frustration. The exchange between nearest-neighbour (NN) metals in successive bilayers ( $J_{c1}$ ) (separated by an oxygen vacancy) is antiferromagnetic. Perpendicular to the  $c$  axis (as dictated by the Goodenough-Kanamori (GK) rules [13,14]),  $J_{ab}$  exchanges due to NN Cu-Cu, Fe-Cu and Fe-Fe pairs in the  $ab$  plane are

\*Contact author: [garcia.munoz@icmab.es](mailto:garcia.munoz@icmab.es)

Published by the American Physical Society under the terms of the [Creative Commons Attribution 4.0 International license](https://creativecommons.org/licenses/by/4.0/). Further distribution of this work must maintain attribution to the author(s) and the published article's title, journal citation, and DOI.

all antiferromagnetic [9]. In the presence of Fe/Cu disorder, a collinear  $\mathbf{k}_1 = (1/2, 1/2, 1/2)$  phase ( $T_{N1}$ ) transforms into an incommensurate spiral order ( $\mathbf{k}_2 = (1/2, 1/2, 1/2 \pm q)$ ) at  $T_S < T_{N1}$ . Raising the fraction of  $\text{Fe}^{3+}\text{Fe}^{3+}\text{O}_9$  bipyramids in more disordered samples, the spiral transition temperature can be tuned by more than 180 K ( $\Delta T_S$ ) [10,12].

A central issue is finding the most efficient way to upgrade the magnetic features and potential magnetoelectric response associated with the spiral ordering in these  $AA'BB'O_5$  (oxygen deficient) double-perovskites ( $A = \text{R}^{3+}$ ,  $A' = \text{Ba}^{2+}$ ,  $\text{B}^{2+} = \text{Cu}^{2+}$ ,  $\text{B}^{3+} = \text{Fe}^{3+}$ ). On the one hand, by manipulating the Cu/Fe disorder, the highest spiral-ordering temperature reported in YBCFO is  $T_S \approx 366$  K, achieved by quenching the material in water after the last annealing [12]. On the other hand, the strategy solely based on disorder has some limitations and drawbacks. For instance, (i) faster cooling rates are difficult to meet; (ii) a too high density of Fe/Fe bipyramids favors magnetic phase separation; (iii) it is difficult to monitor, manipulate and reproduce relevant features of the spiral (such as its orientation or cycloidal component); (iv) the lossy dielectric behavior of highly disordered polycrystalline samples; or (v) the fact that typically, B-site disorder in as-grown single crystals is too low. Therefore, exploring new strategies can be crucial to manipulate and optimize the characteristics and potential properties of these unique high- $T_S$  spiral compounds.

The studies aimed at tuning the balance between magnetic interactions in this system are still scarce. With regard to the application of chemical pressure (by means of chemical substitutions), previous reports were mainly focused on substitutions at the  $AA'$ -sites ( $\text{R}^{3+}$ ,  $\text{Ba}^{2+}$ ) of the double perovskite. Thus, in  $\text{RBaCuFeO}_5$  compounds the smallest  $\text{R}^{3+}$  rare-earths decrease  $T_S$ , while the bigger-size ones end up by creating defects in the stacking of  $\text{R}^{3+}$  and  $\text{Ba}^{2+}$  layers. In  $\text{YBa}_{1-x}\text{Sr}_x\text{CuFeO}_5$  compounds, where the divalent  $A' = \text{Ba}^{2+}$  ion is substituted with the smaller  $\text{Sr}^{2+}$ , the changes in the interatomic distances parallel to  $c$  between transition metal atoms (M: Cu, Fe) modify the exchange interactions and extend the spiral ordering up to  $T_S \approx 375$  (3) K. But, on another hand, the lack of polarization in Sr-doped YBCFO was attributed to a negligible DM contribution due to a spiral orientation of the moments parallel to the tetragonal plane [15,16].

Concerning B-sites substitutions, a decrease in the number of  $\text{Fe}^{3+}$  ions brings about a severe drop of the spiral transition temperature [17]. This was experimentally disclosed by Zhang *et al.* [17] when trying to enhance the spin-orbit coupling in the system. For that, highly symmetric  $\text{Fe}^{3+}$  ions ( $3d^5$ ,  $L = 0$ ,  $S = 5/2$ ) were partially substituted with  $3d^4$   $\text{Mn}^{3+}$  ions ( $L = 2$ ,  $S = 2$ ) in  $\text{YBaCu}(\text{Fe}, \text{Mn})\text{O}_5$  compounds. Three critical aspects to consider when applying chemical pressure to YBCFO are: (i) the lattice and steric effects (impact on the interatomic distances), (ii) the changes in the sign and strength of the magnetic interactions (impact on magnetic terms), and (iii) the changes in the spin-orbit coupling (impact on magnetic anisotropy).

The substitution of  $\text{Cu}^{2+}$  forming elongated square  $\text{CuO}_5$  pyramids with divalent high-spin (HS)  $\text{Co}^{2+}$  ions is one of the most attractive. On one hand, it does not reduce the number of Fe atoms as it concerns the divalent B position, and

the  $\text{Cu}^{2+}$  and HS  $\text{Co}^{2+}$  ionic sizes are not very different. Additionally, the high-spin electronic configuration of  $\text{Co}^{2+}$  ( $t_{2g}^5 e_g^2$ ) is compatible with regular (even flattened) pyramids in five coordination and does not require axially elongated  $\text{CoO}_5$  pyramids [18]. Moreover, it exhibits both a spin and an appreciable orbital component. HS  $\text{Co}^{2+}$  is known to exhibit a large amount of mixing between levels due to spin-orbit interaction, which favors a non-negligible orbital contribution and an appreciable single-ion magnetic anisotropy [19]. This study explores the incidence of the  $\text{Cu}^{2+}$  with  $\text{Co}^{2+}$  substitution on the high- $T_S$  spiral phase of YBCFO. A new avenue to upgrade the stability and properties of the singular chiral magnetic state of YBCFO is presented, based on the manipulation of the characteristic elongation of  $\text{Cu}^{2+}\text{O}_5$  pyramids in this family of promising perovskites.

## II. SAMPLE PREPARATION AND EXPERIMENTAL METHODS

$\text{YBa}(\text{Cu}_{1-x}\text{Co}_x)\text{FeO}_5$  polycrystalline samples with cobalt contents  $x = 0.01, 0.03, 0.04, 0.05, 0.06, 0.065$  and  $0.075$  were successfully prepared by solid-state reaction. The synthesis process was similar to the one described in Ref. [12] for YBCFO samples. First of all, a preannealing process was conducted on  $\text{Y}_2\text{O}_3$  at  $900^\circ\text{C}$  for 10 h to promote its decarbonation. The rest of high-purity precursors ( $\text{BaCO}_3$ ,  $\text{CuO}$ ,  $\text{Fe}_2\text{O}_3$ , and  $\text{Co}_3\text{O}_4$ ) were dehydrated at  $150^\circ\text{C}$  for 48 h. Stoichiometric amounts of the high purity precursors  $\text{Y}_2\text{O}_3$ ,  $\text{BaCO}_3$ ,  $\text{CuO}$ ,  $\text{Fe}_2\text{O}_3$ , and  $\text{Co}_3\text{O}_4$  were used. Then all precursors were thoroughly mixed and grounded using an automatic agate mortar, and the obtained powder was subsequently pressed into pellets and sintered at  $1100^\circ\text{C}$  for 50 h in air. Finally, the same cooling process to room temperature was applied to all the samples inside the furnace at a controlled rate of 300 K/h. Sample quality was firstly characterized by laboratory x-ray powder diffraction using a Siemens D-5000 diffractometer ( $\lambda[\text{CuK}\alpha] = 1.54 \text{ \AA}$ ), showing no secondary phases within the detection limit of the technique ( $\sim 1\%$ ). Hereafter samples are denoted as Co-0%, Co-1%, Co-3%, Co-4%, Co-5%, Co-6%, Co-6.5% and Co-7.5%. We previously characterized the Co-0% sample in Ref. [7], here used for the sake of comparison. Synchrotron and neutron diffraction measurements further confirmed the good quality of the samples. Macroscopic magnetic measurements were performed using a Superconducting Quantum Interference Magnetometer Device and a Vibrating Sample Magnetometer (VSM) adapted to a Physical Properties Measurement System, both from Quantum Design Inc. The VSM was used to cover the interval 300–550 K. Synchrotron x-ray powder diffraction (SXRPD) were collected at the BL04-MSPD beamline [20] of the ALBA Synchrotron Light Facility (Cerdanyola del Valles, Spain). As detection system we used a high-throughput position-sensitive detector MYTHEN (90 s per pattern acquisition time/pattern). A short wavelength,  $\lambda = 0.41338$  (3)  $\text{ \AA}$  was selected to reduce absorption and enlarge the  $q$  range (NIST standard silicon was used for calibration). The powder samples were loaded in borosilicate glass capillaries (0.7 mm diameter) and kept spinning during data acquisition. We also performed x-ray absorption spectroscopy measurements (XAS) across the Co  $L_{2,3}$  and Fe  $L_{2,3}$  edges on

TABLE I. Refined interatomic distances (in Angstroms) as yielded by the analysis of synchrotron x-ray diffraction data at 300 K ( $\lambda = 0.41338 \text{ \AA}$ ). (H: height of the pyramid). (\*: minority fraction;  $n_d$  (disorder) = Occ (Fe1\*/[Cu,Co]2\*)).

YBaCu <sub>1-x</sub> Co <sub>x</sub> FeO <sub>5</sub> (300 K/h cooling)	Co-1%	Co-3%	Co-4%	Co-5%	Co-6%	Co-6.5%	Co-7.5%	Co-15%	Co-25%
$1-n_d = \text{Occ (Cu,Co)1/Fe2}$	0.639 (20)	0.638 (20)	0.637 (20)	0.632 (20)	0.632 (20)	0.634 (20)	0.631 (20)	0.632 (20)	0.630 (20)
$n_d = \text{Occ Fe1*/(Cu,Co)2*}$	0.361 (20)	0.362 (20)	0.363 (20)	0.368 (20)	0.368 (20)	0.366 (20)	0.369 (20)	0.368 (20)	0.370 (20)
$d_s$ (Å)	2.826 (10)	2.827 (10)	2.827 (13)	2.828 (11)	2.828 (14)	2.830 (13)	2.831 (11)	2.841 (13)	2.851 (12)
$d_t$ (Å)	4.837 (10)	4.834 (10)	4.832 (13)	4.830 (11)	4.828 (14)	4.826 (13)	4.826 (11)	4.806 (13)	4.785 (12)
$d_t/d_s$	1.7116 (71)	1.7099 (73)	1.7092 (88)	1.7079 (77)	1.7072 (71)	1.7053 (91)	1.7047 (76)	1.6918 (90)	1.6780 (85)
$H_L$ (Å)	2.474 (19)	2.469 (20)	2.467 (20)	2.462 (23)	2.459 (22)	2.458 (22)	2.454 (21)	2.429 (22)	2.401 (19)
$H_S$ (Å)	2.362 (19)	2.365 (20)	2.365 (20)	2.367 (23)	2.369 (22)	2.370 (22)	2.372 (21)	2.377 (22)	2.384 (19)
$d((\text{Cu, Co})\text{I} - \text{O1})_{\text{apical}}$ (Å)	2.158 (10)	2.155 (11)	2.154 (10)	2.151 (13)	2.146 (12)	2.144 (12)	2.140 (12)	2.131 (20)	2.119 (17)
$d((\text{Cu, Co})\text{I} - \text{O3})_{\text{basal}}$ (Å)	1.963 (3)	1.963 (3)	1.963 (2)	1.962 (3)	1.963 (3)	1.962 (3)	1.964 (4)	1.963 (4)	1.962 (2)
$d(\text{Fe2} - \text{O1})_{\text{apical}}$ (Å)	1.903 (10)	1.906 (11)	1.907 (11)	1.910 (14)	1.913 (13)	1.915 (13)	1.917 (13)	1.922 (21)	1.928 (17)
$d(\text{Fe2} - \text{O2})_{\text{basal}}$ (Å)	1.991 (4)	1.991 (4)	1.991 (4)	1.991 (4)	1.991 (4)	1.991 (4)	1.991 (4)	1.922 (21)	1.928 (17)

some of the samples, by using the HECTOR cryomagnet end-station at the BL29-BOREAS beamline of ALBA [21]. The XAS spectra confirmed the divalent oxidation state of Co ions in these compounds and hence the Cu with Co isovalent substitution. Neutron powder diffraction (NPD) was performed at the high-flux reactor of the Institut Laue Langevin (Grenoble, France) using the high intensity diffractometer D1B with  $\lambda = 2.52 \text{ \AA}$ . NPD patterns were collected for  $x \leq 7.5\%$  Co at fixed selected temperatures and also in continuous mode following temperature ramps within the 10–500 K range (heating rate of 2 K/min).

Later on, in a second process of synthesis, were prepared two additional (highly-doped) compositions (Co-15% and Co-25%), following the same protocol as for  $x \leq 7.5\%$  Co samples. These two highly-doped specimens were characterized by SXRPD. Structural and magnetic refinements (detailed in Tables I, II and, as Supplemental Material (SM),

in Tables S1, S2, and S3) were executed using the FULLPROF suite program [22]. Illustrations of the crystal and magnetic structures were done using the VESTA program [23].

### III. RESULTS

#### A. Isovalent Cu<sup>2+</sup>/Co<sup>2+</sup> substitution

Refined SXRPD patterns are shown in Figs. 1(a) and 1(b) and Fig. S1 (SM, Ref. [24]). The expected divalent oxidation state of Co ions was confirmed by XAS measurements, performed on Co1% and Co5% compounds, taken as representative samples of the set. We measured their room temperature x-ray absorption spectra across the Co and Fe  $L_{2,3}$  edges, as plotted in Figs. 1(c) and 1(d), respectively. The inset of Fig. 1(c) shows that the Co  $L_3$  edge is clearly distinguishable from the Ba  $M_5$  edge tail. The much higher intensity of the absorption peaks from Ba is due to the larger

TABLE II. Refined magnetic parameters obtained from neutron data of YBaCu<sub>1-x</sub>Co<sub>x</sub>FeO<sub>5</sub> samples (300 K/h cooling) at T = 10 K. The average magnetic moments  $m_S$  and  $m_L$  at the Fe-rich and Cu-rich pyramid sites were obtained imposing  $m_L = r m_S$ , with the ratio r calculated according to the refined cationic distribution.  $f_m$  refers to the % of the magnetic phase. AF1, AF2, and AF3 orders, respectively, display propagation vectors  $\mathbf{k}_1 = (1/2, 1/2, 1/2)$ ,  $\mathbf{k}_2 = (1/2, 1/2, 1/2 \pm q)$  and  $\mathbf{k}_3 = (1/2, 1/2, 0)$ .

YBaCu <sub>1-x</sub> Co <sub>x</sub> FeO <sub>5</sub>	Co-0%	Co-1%	Co-3%	Co-4%	Co-5%	Co-6%	Co-6.5%	Co-7.5%
$T_{N1}$ (K)	445 (9)	447 (8)	425 (8)	420 (8)	413 (8)	403 (10)	390 (12)	370 (12)
$T_{N2} = T_S$ (K)	249 (9)	236 (8)	277 (8)	296 (8)	320 (8)	350 (8)	355 (10)	-
$T_{N3}$ (K)	-	-	-	-	320 (8)	350 (10)	355 (12)	362 (12)
COLLINEAR (AF1)								
$f_m(\mathbf{k}_1)$ (%)	20.7 (1.1)	17.4 (3.0)	19.8 (2.6)	16.9 (2.7)	23.2 (1.7)	22.3 (2.0)	39.3 (1.2)	55.0 (0.8)
$\theta_{C1}$ (deg)	52 (8)	42 (9)	45 (6)	51 (10)	44 (3)	40 (4)	56 (2)	52 (2)
SPIRAL (AF2) $M_R = M_I$								
$f_m(\mathbf{k}_2)$ (%)	79.3 (1.1)	82.6 (1.7)	80.2 (1.5)	75.2 (1.6)	61.1 (1.0)	61.8 (1.1)	32.4 (0.6)	0
$\theta_S$ (deg)	42 (5)	43 (3)	38 (3)	31 (5)	26 (3)	16 (5)	13 (6)	-
$q_S$ (r.l.u.)	0.119 (3)	0.117 (2)	0.134 (2)	0.147 (2)	0.160 (2)	0.176 (2)	0.177 (2)	-
COLLINEAR (AF3)								
$f_m(\mathbf{k}_3)$ (%)	0	0	0	7.9 (3.0)	15.7 (2.8)	16.0 (2.8)	28.3 (1.3)	45.0 (0.9)
$\theta_{C3}$ (deg)	-	-	-	66 (96)	94 (60)	94 (60)	77 (8)	78 (6)
$r = m_L/m_2$	0.606 (48)	0.687 (52)	0.689 (52)	0.691 (51)	0.701 (49)	0.701 (49)	0.697 (50)	0.703 (49)
$m_1$ ( $\mu_B$ )	2.418 (25)	2.532 (56)	2.659 (50)	2.684 (61)	3.109 (45)	3.109 (45)	2.873 (46)	2.958 (33)
$m_2 = r m_1$ ( $\mu_B$ )	1.473 (15)	1.741 (50)	1.770 (44)	1.855 (55)	2.178 (40)	2.013 (40)	2.061 (27)	1.664 (15)

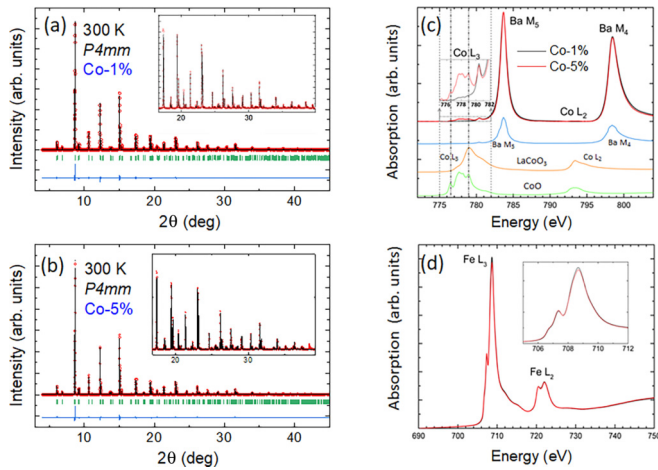


FIG. 1. Synchrotron diffraction: (a), (b) Rietveld refinement (black curve) of the synchrotron x-ray intensities (red circles) of  $\text{YBa}(\text{Cu}_{1-x}\text{Co}_x)\text{FeO}_5$  ( $x = 0.01$  and  $0.05$ ) at 300 K. Bottom blue line is the observed-calculated difference. Inset: detail of the high-angle region. X-ray absorption (XAS): XAS spectra across (c) the Co  $L_{2,3}$  edges and (d) the Fe  $L_{2,3}$  edges for Co1% and Co5% samples. The insets in (c) and (d) focus on the Co  $L_3$  and Fe  $L_3$  edges, respectively. The reference compounds CoO ( $\text{Co}^{2+}$ ),  $\text{LaCoO}_3$  ( $\text{Co}^{3+}$ ) and  $\text{Ba}_{1.60}\text{Ce}_{0.20}\text{Na}_{0.20}\text{Ca}(\text{BO}_3)_2$  ( $\text{Ba}^{2+}$ ) are shown for comparison.

absorption cross sections of the Ba  $M_{4,5}$  transitions and a far higher relative fraction of Ba in the samples. As shown in Fig. 1(c) the XAS energy positions and structure of the experimental Co  $L_3$  edge in the samples match well those found in CoO, a prototypical  $\text{Co}^{2+}$  compound. XAS thus confirmed that the  $\text{Co}^{2+}$  for  $\text{Cu}^{2+}$  chemical substitution was indeed isovalent, and that cobalt ions adopted the divalent HS electronic configuration ( $3d^7: t_{2g}^5 e_g^2$ ). Similarly, we did not appreciate any hint of a mixed or intermediate valence in Fe cations. The Fe XAS spectra shown in Fig. 1(d) ( $L_{2,3}$  edges) indicate a stable +3 valence state for Fe.

### B. Evaluation of cation disorder

As previously mentioned, the degree of divalent/trivalent chemical disorder has a direct impact on the level of magnetic frustration in this system [12,25]. First of all, we have investigated the possible effects of the Cu/Co substitution on the B-site disorder.  $\text{Cu}^{2+}/\text{Fe}^{3+}$  disorder is at the origin of magnetic frustration and the stabilization of the spiral ordering in YBCFO. In absence of disorder this layered structure is not geometrically frustrated. In YBCFO Fe/Cu disorder is parametrized by the improper occupancy  $n_d$ , which is defined as the fractional occupancy of the minority ions in the upper or lower pyramids, indistinctly [i.e.,  $n_d = \text{Occ Fe}^* = \text{Occ}(\text{Cu,Co})2^*$ ]. Notice that it is not possible to refine the atomic coordinates and individual occupations of  $\text{Cu}^{2+}$ ,  $\text{Co}^{2+}$  and  $\text{Fe}^{3+}$  ions independently. Even more so in view of the very small fraction of Co in the compounds. As described in the next section, the best approximation is refining independent coordinates and the corresponding occupations for trivalent (Fe) and divalent (Cu,Co) species, respectively. The values for the latter being average values that do not distinguish between Cu and Co. The refined Fe/(Cu/Co) fractional occupations at

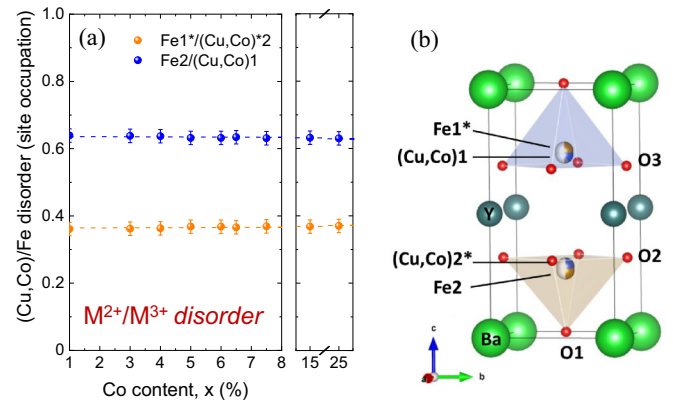


FIG. 2. (a) B-site chemical disorder in  $\text{YBaCu}_{1-x}\text{Co}_x\text{FeO}_5$  samples. Refined proper (blue) and improper (brown,  $n_d$ ) occupations. (b) Scheme of the unit cell. In the structure, (Cu,Co)1 atoms are in the upper pyramid (together with improper Fe1\*), and Fe2 atoms occupy the lower one (together with improper (Cu,Co)2\*) (\* indicates the minority fraction site).

the M1 and M2 pyramids in our  $\text{YBaCu}_{1-x}\text{Co}_x\text{FeO}_5$  samples are plotted in Fig. 2 and reported in Table I. They show that disorder keeps invariant in our samples, which were prepared under identical conditions (same annealing temperature and under the same cooling rate). We have found a mean disorder value of  $\sim 36\%$ , independent (within error) of the Co content (see Table I and Fig. 2).

### C. Structural study by synchrotron diffraction

Samples were single phased and all SXRPD patterns were satisfactorily refined using the expected  $P4mm$  symmetry. The structural parameters and corresponding agreement factors refined at 300 K are reported in Tables S1 and S3 (SM, Ref. [24]). There are two pyramids in the unit cell:  $[\text{Cu}/\text{Co}]^{2+}$ -rich is the upper pyramid (M1 site) and the Fe-rich is the lower (M2 site) pyramid. From synchrotron data we refined the atomic positions and the occupancies of the divalent  $[\text{Cu}/\text{Co}]^{2+}$  and trivalent  $\text{Fe}^{3+}$  ions in the two pyramids of the unit cell. As highlighted in preceding paragraphs the partial substitution of  $\text{Cu}^{2+}$  with  $\text{Co}^{2+}$  does not produce any additional chemical disorder of divalent/trivalent ions in the bipyramidal layers. Namely, the divalent/trivalent chemical disorder is independent of the Co content in our samples, synthesized following an identical process.

SXRPD patterns allowed refining the two atomic positions and the occupancies of the Cu/Co and Fe ions, separately, in each pyramid of the unit cell: the upper (blue and Cu-rich, M1 site) and the lower (brown and Fe-rich, M2 site) pyramids, respectively. For this purpose, the  $z$  coordinates of the two positions that a given metal M (either Fe or Cu) can occupy in the cell (M1 and M2) were constrained in the form  $z(\text{M1}) + z(\text{M2}) = 1$ .

As shown in Fig. S2 (SM, Ref. [24]), a linear expansion of  $a(=b)$  when Cu gets substituted with Co produces a small expansion of the unit cell volume, which is not surprising attending to the slightly larger ionic effective radius of  $\text{Co}^{2+}$  ( $0.67 \text{ \AA}$  in V coordination, HS) as compared to  $\text{Cu}^{2+}$  ( $0.65 \text{ \AA}$  in V coordination [26]). However, this evolution is at odds

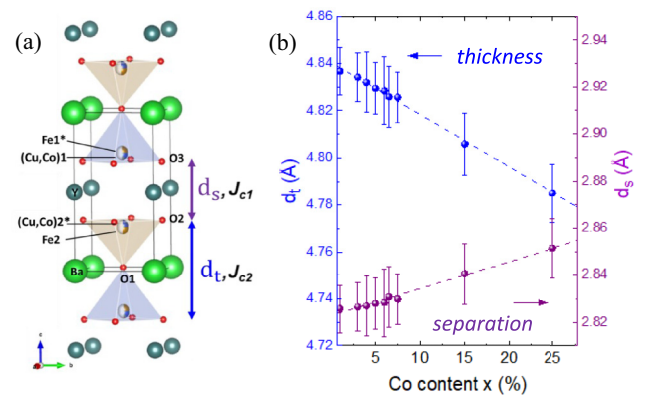


with the contraction observed in the  $c$  parameter, which also contributes to a linear reduction of the tetragonal distortion ( $\Delta_T \equiv c/2a$ ) (see Fig. S2 (SM, Ref. [24])). We will show next that the contraction of the unit cell dimension parallel to the  $c$  axis is of paramount importance. A contraction was also observed in pure YBCFO by increasing B-site disorder [12], namely, in a scenario totally different to the present one, because here the level of cation disorder keeps invariant. Therefore, the creation of new frustrating bonds (an increasing number of frustrated  $\text{Fe}_2\text{O}_9$  bipyramids in the layered structure) does not occur here and cannot be used to justify the huge rise in the thermal stability of the spiral as revealed by neutrons.

In the YBCFO structure,  $c$  is governed by two key distances ( $c = d_t + d_s$ ) that are shown in Fig. 3(a): the thickness of the bipyramidal layer ( $d_t$ ) and the separation between bilayers ( $d_s$ ). The  $\text{Ba}^{2+}$  ions are located within the bilayer spacing ( $d_t$ ), whereas  $\text{CuFeO}_9$  bilayers of corner-sharing pyramids are separated by  $\text{Y}^{3+}$  layers. Figure 3(b) illustrates the compression of the thickness  $d_t$  by increasing the presence of Co, so that the raise in the distance between adjacent bilayers along  $c$  ( $d_s$ ) cannot compensate the contraction in the  $\text{CuFeO}_9$  bilayers, resulting in the overall contraction of the  $c$ -parameter.

The observed trend in the evolution of  $d_t$  versus Co is of utmost importance and demands a more in-depth analysis. For more clarity, Figs. 3(c) and 3(d), respectively, show the evolution of the average Cu-O and Fe-O interatomic distances in the two pyramids. With regards to the  $\text{Cu}^{2+}(3d^9)$  ion, the low-symmetry local distortions of  $\text{Cu}^{2+}\text{O}_6$  units typical of high-symmetry (octahedral) sites are a consequence of the Jahn-Teller effect, as a result of the twofold ( $x^2 - y^2, 3z^2 - r^2$ ) orbitally degenerated  $E_g(O_h)$  ground state. In host lattices like YBCFO, where  $\text{Cu}^{2+}$  is in five-coordination with identical ligands, the tetragonal pyramid with a long apical bond distance is the energetically preferred coordination geometry. The uniaxial elongation distortion in the square  $\text{Cu}^{2+}\text{O}_5$  pyramid of YBCFO results from the charge repulsion along  $c$ , triggered by the full electronic occupation of the  $3z^2 - r^2$  orbital in this structure. Moreover, the basal or equatorial Cu-O3 bond lengths are shorter than in the analogous Fe-O2 bonds of the  $\text{Fe}^{3+}\text{O}_5$  pyramid. The main interatomic distances in the structure are gathered in Table I, and the distances displayed in Figs. 3(c) and 3(d) are the M-O bond lengths for the majority metal in each pyramid. So, in Fig. 3(c) [3(d)] distances are taken with respect to the Cu (Fe) position. When introducing cobalt at divalent Cu sites, a look to Fig. 3(c) unveils apparent changes in the bond lengths splitting of  $M^{2+}\text{O}_5$  pyramids. Whereas the basal Cu-O3 or Fe-O2 bonds are hardly modified, the apical Cu-O1 bond (axial elongation) systematically shrinks at a rate  $\sim 1.7 \times 10^{-3} \text{ \AA}/\% \text{Co}$  (almost a  $\approx 2\%$  reduction between 1 and 25% of Co content). The large splitting (difference) between Cu-O1 (apical) and Cu-O3 (basal) pyramidal bond lengths decreases from  $\sim 10\%$  down to the  $\sim 8\%$  in Co-25%, our most heavily Co doped sample. Figure 3(c) thus discloses that the presence of HS  $\text{Co}^{2+}$  ions brings about a noticeable reduction in the elongation of Cu (divalent) pyramids. The O1 atomic shift responsible for the reduction of the uniaxial elongation also explains the growing apical Fe-O1 distance described in Fig. 3(d), although this effect is smaller and in the flattened Fe pyramid the Fe-O1 bond length remains

Evolution of the thickness and separation of the bilayers: compression of the bipyramid



Evolution of the two pyramids: reduction of the axial elongation in  $\text{CuO}_5$

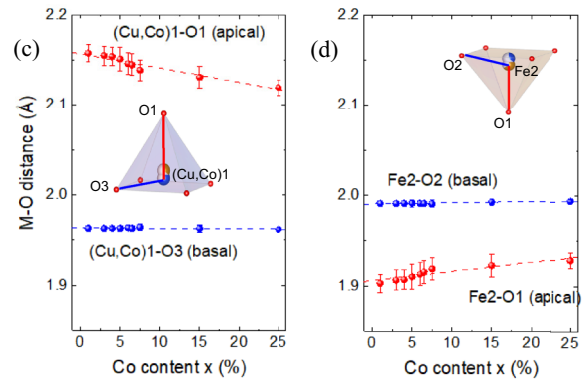


FIG. 3. (Top) Influence of Cu/Co substitution on the thickness and separation of the bilayers. (a) Projection of the YBCFO structure including two successive bipyramids along  $c$ , illustrating the thickness  $d_t$  of a bilayer and the separation  $d_s$  between bilayers. (b) Evolution of the thickness of the bipyramidal layer ( $d_t$ , left axis) and of the separation between bilayers ( $d_s$ , right axis). (Bottom) Evolution of the two pyramids in the cell increasing the fraction of divalent Co. (c) Evolution of the splitting between apical and basal average M-O distances in the elongated Cu-rich square pyramid ( $M = \text{Cu}_{1-x}\text{Co}_x$ ). (d) Fe-O interatomic distances in the Fe-rich pyramid. The evolution of the apical and basal (equatorial) distances (illustrated in the inset) is shown in both pyramids. Dotted lines are linear fits to data points. The marked reduction in the elongation of the Cu-rich pyramid is not compensated by the stretching of the apical Fe2-O1 bond, resulting in a contraction of the  $\text{FeCuO}_9$  bipyramid thickness (bilayer).

always shorter than the basal one (Fe-O2). The heights of the long and short pyramids ( $H_L$  and  $H_s$ ), as defined in Ref. [12] are also given in Table I and shown in Fig. S2 (SM, Ref. [24]). So, the observed structural evolution in  $\text{YBaCu}_{1-x}\text{Co}_x\text{FeO}_5$  indicates that the electronic configuration of the  $3d^7$  divalent substituting ions (in pyramidal coordination, with unoccupied states of  $3z^2 - r^2$  character), is at the origin and is the cause of the slimming observed in  $d_t$ , the thickness of the bipyramidal layer.

As we are showing hereunder, a closer look to the impact of Co uncovers the extraordinary importance that the uniaxial elongation distortion of  $\text{Cu}^{2+}$  ions in pyramidal units has for the stability of the chiral magnetic ordering and the

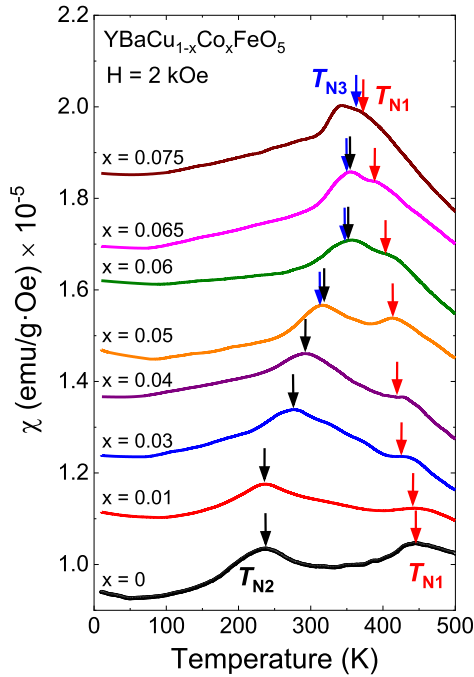


FIG. 4. Magnetic susceptibility curves (measured in FC, 2 kOe) for  $\text{YBaCu}_{1-x}\text{Co}_x\text{FeO}_5$  samples. Evolution with increasing the fraction  $x$  of divalent Co sites. Successive curves were shifted by  $+10^{-6}\text{emu g}^{-1}\text{Oe}^{-1}$  for clarity. Arrows signal the onset temperature for AF1 (red), AF2 (black) and AF3 (blue) ordering according to neutron diffraction.

multiferroic properties of the high- $T_S$  family of  $\text{RBaCuFeO}_5$  double perovskites.

#### D. Magnetic phase diagram driven by divalent Co

The magnetic transition temperatures in  $\text{YBaCu}_{1-x}\text{Co}_x\text{FeO}_5$  were identified by susceptibility [ $\chi(T)$ ] and NPD measurements. The corresponding transition temperatures are shown in Table II. The  $\chi(T)$  curves of Fig. 4 were measured in a warming ramp under a field of 2 kOe in field-cooling (FC) conditions. As indicated in the figure, two local maxima in  $\chi(T)$  identify the transitions associated to collinear antiferromagnetic AF1 and spiral AF2 orders. In addition, we will show that neutron data reveals the progressive appearance of AF3 domains as Co doping approaches the critical value  $x \approx 7.5\%$ , around which the spiral phase is no longer formed. For  $x \approx 7.5\%$  the susceptibility peaks have merged into one, and the two final coexisting magnetic phases are the collinear AF1 and AF3 orders.

The magnetic evolution is more clearly disclosed by the neutron measurements shown in Figs. 5 and 6. The low-angle region of the NPD patterns collected at 10 K is shown in Fig. 5(a). With regards to the temperature ( $T$ ) evolution, Fig. 6(a) shows the  $T$ - $Q$  projections of the NPD intensities collected between 10 and 500 K, where the onset and evolution of the AF1, AF2, and AF3 magnetic phases is clearly visible.  $T_S (= T_{N2})$  and the spiral ordering get easily identifiable by the appearance of a set of incommensurate magnetic satellites with propagation vector  $\mathbf{k}_2 = (1/2, 1/2, 1/2 \pm q)$ .

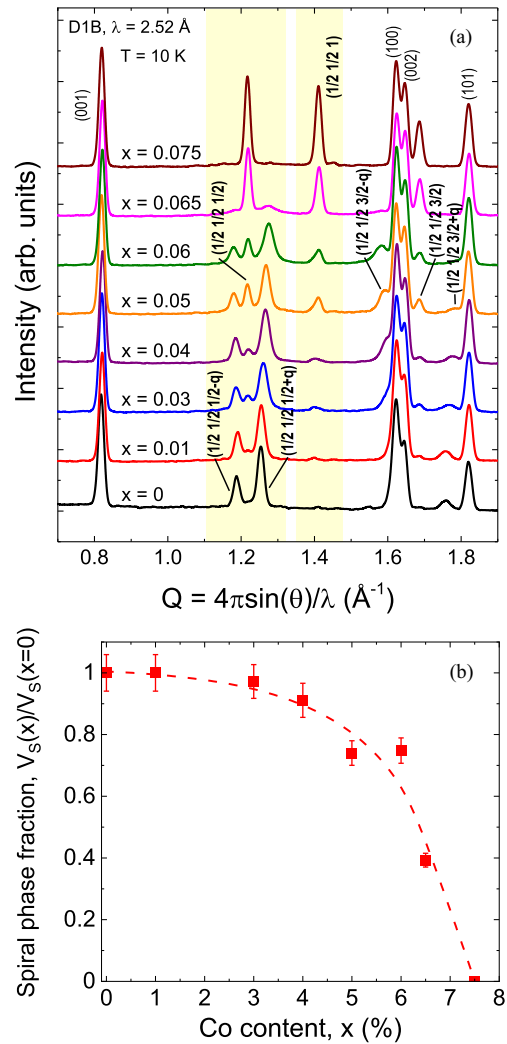


FIG. 5. (a) Low- $Q$  region of the neutron patterns taken at 10 K in  $\text{YBaCu}_{1-x}\text{Co}_x\text{FeO}_5$  samples with increasing fractions of Cu/Co substitution (D1B@ILL). (b) Co content dependence of the fraction of the incommensurate spiral phase (AF2) found at  $T = 10\text{ K}$  as a function of Co in  $\text{YBaCu}_{1-x}\text{Co}_x\text{FeO}_5$ .

Upon raising Co, we observe a huge expansion of the thermal stability range of the spiral phase, from  $T_S = 210\text{ K}$  up to 355 K, comfortably far beyond RT. At this point we draw attention to the fact that such spiral transition temperature is remarkably and unexpectedly high because cation disorder in our samples is rather low and held constant [12].

A glance to Figs. 5 and 6 reveals that increasing the Co fraction above 5–6% there is a progressive suppression of the incommensurate spiral domains in favor of the  $\mathbf{k}_1 = (1/2, 1/2, 1/2)$  peaks (AF1) and of a second collinear phase with  $\mathbf{k}_3 = (1/2, 1/2, 0)$  (AF3 phase), below  $T_S$ . More quantitatively, we have plotted in Fig. 5(b) the evolution of the spiral phase fraction (10 K) when increasing Co content up to  $x = 7.5\%$  on the basis of neutron data recorded at the base temperature.

The evolution of the magnetic transition temperatures with increasing Co doping is displayed in the  $x_{\text{Co}}-T$  phase diagram of Fig. 7. The general trends observed in the phase diagram

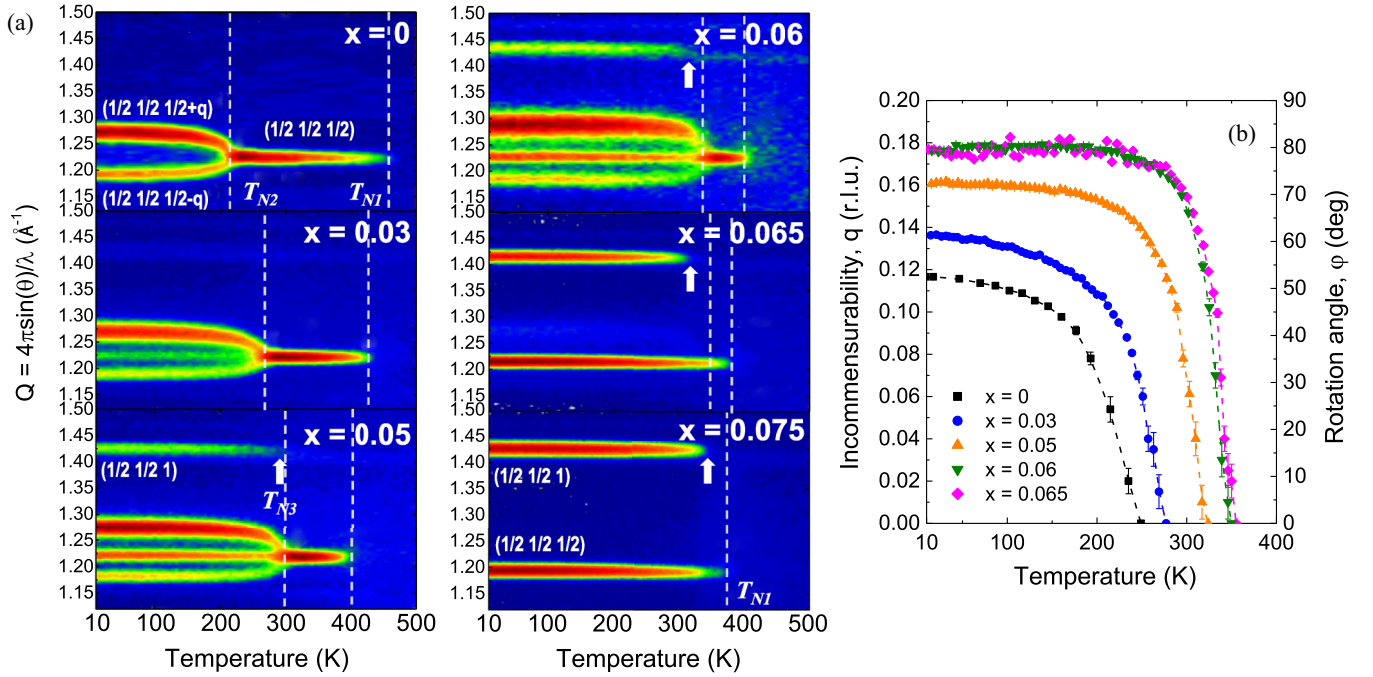


FIG. 6. (a) Contour maps of the neutron-diffracted intensities in  $\text{YBaCu}_{1-x}\text{Co}_x\text{FeO}_5$ . T-Q projection showing the thermal evolution of the main magnetic reflections. For  $x \geq 5\%$  the spiral order (AF2) coexists with gradually higher AF1 and AF3 reflections. For  $x = 7.5\%$  the AF1 and AF3 phases dominate and the spiral order has been suppressed. Vertical dashed lines indicate the onset of AF1 ( $T_{N1}$ ) and AF2 ( $T_{N2}$ ) phases, and white arrows signal the emergence of AF3 domains ( $T_{N3}$ ). (b) Influence of Co content on the incommensuration  $q_S$  of the spiral phase and its temperature dependence. The latter clearly illustrate the spiral transition temperatures. The dashed lines are guides to the eye.

inserting cobalt are reminiscent of the  $n_d$ - $T$  phase diagram of YBCFO, driven by increasing disorder [10,12]. This confirms the efficacy of the new strategy, based on acting over the axial elongation at the “nominal” Cu pyramids, to tune and enhance magnetic frustration in the material.

A triple point is also achieved in  $\text{YBaCu}_{1-x}\text{Co}_x\text{FeO}_5$ , when  $x \approx 7.5\%$ , for which we have identified the critical values ( $q_s^c = 0.177(3)$  r.l.u. and  $T_s^c = \sim 360$  K). Beyond the triple point, the two types of coexisting collinear phases (AF1 and AF3) are the characteristic ones of the phase separation region in YBCFO [12,27]. In the phase diagram of YBCFO (driven by Cu/Fe disorder), the phase separation region emerges immediately beyond the triple critical point ( $q_s^c = 0.186(13)$  r.l.u. and  $T_s^c = 407(16)$  K in YBCFO [12]). We have also shown that, in  $\text{YBaCu}_{1-x}\text{Co}_x\text{FeO}_5$ , Co ions progressively favor the presence of AF3 domains even before the tricritical point (Co-induced phase separation). In agreement with the GK rules [13,14], the replacement of bipyramids based on FM  $\text{Cu}^{2+}/\text{Fe}^{2+}$  pairs with AF  $\text{Co}^{2+}/\text{Fe}^{2+}$  (or  $\text{Co}^{2+}/\text{Cu}^{2+}$ ) dimers (in  $\text{CoMO}_9$  bipyramids) favors the emergence of collinear AF regions with  $k_z = 0$  translational symmetry (AF3).

### E. Impact of Co doping on the easy axis and magnetic anisotropy

With the aim of deepening further on the impact of Co doping we performed accurate refinements of the D1B neutron patterns collected (with high statistics) at base temperature (10 K). These refinements are exposed in Fig. S3 (SM, Ref. [24]). All magnetic phases detected in the patterns were

properly fitted. The refined values of the magnetic parameters for the spiral and collinear phases are listed in Table II. It is worth mentioning that the ordered magnetic moments at the nominal Cu and Fe sites ( $m_L$  and  $m_S$ , respectively) were refined imposing  $m_L = r m_S$ , where the ratio  $r$  (as described in Ref. [12]) was calculated according to the cation disorder  $n_d$  refined for each sample:

$$r \equiv m_L/m_S = (1 + 4n_d)/(5 - 4n_d) \quad (1)$$

where  $m_L$  and  $m_S$  are the ordered magnetic moments refined at the long (Cu,Co) and short (Fe) pyramids, respectively. Given the low Co-doping level, for simplicity the theoretical ratio  $m(\text{Fe}^{3+})/m(\text{Cu}^{2+}) = 5$  was imposed in Eq. (1).

A most interesting feature is the orientation of the rotation plane of the spins in the spiral magnetic order.  $M_R$  (R: real) and  $M_I$  (I: imaginary) are the orthogonal amplitudes of the elliptical envelope describing the rotating magnetic moments along  $c$  in the spiral phase. The incommensurate ordering was refined using a circular spiral model ( $M_R = M_I$ ) in which the polar angle  $\theta_S$  was fixed to its refined value using the limit  $M_I \sim 0$ , following the same procedure as in Ref. [12]. As explained there, a proper study of possible changes in the ellipticity would require single crystals. In Table II, the inclination angle  $\theta$  indicates the angular distance between the direction of magnetic spins and the  $c$  axis, as shown in Fig. 8(b). The inclination angles of the magnetic easy axis obtained at 10 K for the spiral and collinear phases ( $\theta_S, \theta_C$ ) are listed in Table II. It is worth remembering that due to the tetragonal symmetry of the parent cell, it is not possible to determine the orientation of the easy axis component parallel to the  $ab$  plane from NPD. Figure S4 (SM, Ref. [24]) plots the



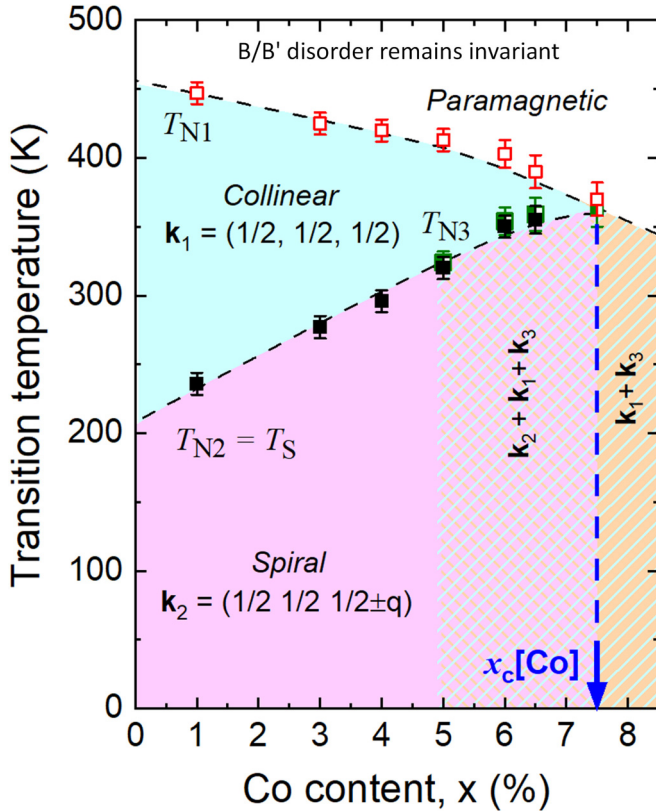


FIG. 7. Magnetic phase diagram versus the Cu/Co substitution rate in YBCFO. The level of  $M^{2+}/Fe^{3+}$  chemical disorder at the B site is kept invariant. The phase boundaries describe the onset of the magnetic phases according to neutron diffraction data. The reduction, provoked by Co doping, of the outstanding uniaxial elongation in  $CuO_5$  pyramids is the driving force of this phase diagram, being able to rise  $T_S$  by  $\sim 150$  K and finally bringing the system to a critical point where the spiral collapses. As revealed in Figs. 5(b) and 6, the fraction of spiral domains decreases for  $x \geq 5\%$  Co in favor of AF1 and mainly AF3 domains ( $T_{N3}$  points in green).

projections of the incommensurate magnetic orders refined at 10 K for all the studied compositions. A comparison of the different sequences of magnetic couplings between neighboring spins along  $c$  in the collinear AF1 and AF3 magnetic orders is shown in the Fig. 9, which also exposes the noncollinear arrangement in the AF2 phase.

Figure 8(a) plots the evolution of  $\theta_S$  (the inclination of the spiral) when increasing the Co fraction. The figure unveils a noteworthy finding consisting in a systematic reorientation of the magnetic spiral upon raising the Cu/Co substitution rate. It is of utmost importance that cobalt decreases the tilting angle  $\theta_S$ , thus favoring the cycloidal component of the spiral at the expense of the helicoidal one. So, we found a huge reorientation ( $\Delta\theta_S \approx -30^\circ$ ) of the spiral plane towards the  $c$  axis that produces a nearly pure cycloidal spin ordering at Co dopings  $x \approx 6.5\%$ . We also notice that, due to the small fraction of commensurate domains at 10 K, their associated errors in Table II make it difficult to draw conclusions on the evolution of the orientation of the collinear moments.

It is also of interest to underline that Fig. 8(c) [inset] reveals a linear correspondence between the incommensura-

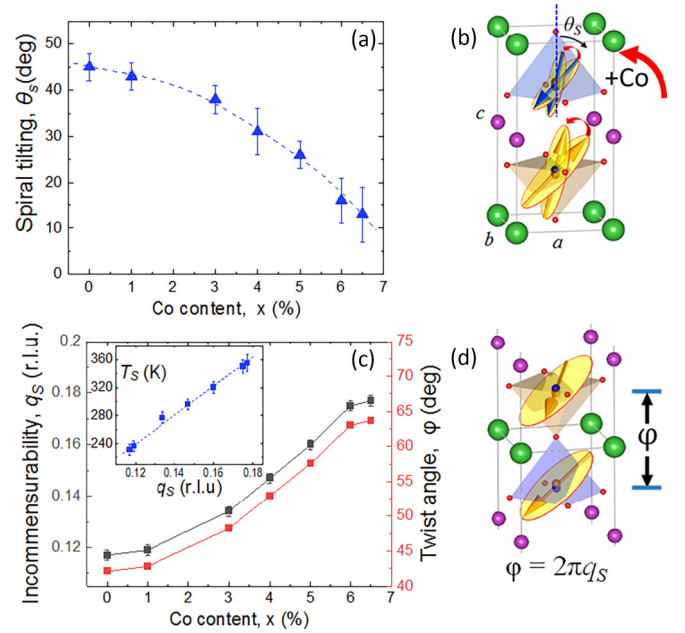


FIG. 8. (a) Changes in the inclination angle  $\theta_S$  of the spiral with Co content (10 K). (b) Sketch showing the rotation of the magnetic spiral plane by Cu/Co substitution (gain of cycloidal component). (c) Evolution of the incommensurate modulation  $q_S$  in the spiral phase (black symbols, left-axis) and of the twist angle  $\varphi = 2\pi q_S$  between the two spins in a bipyramid (red symbols, right-axis). Inset: Linear dependence of the spiral transition temperature ( $T_S$ ) with the modulation  $q_S$  induced by Co doping. (d) Sketch showing the twist angle  $\varphi$  between the moments in a bipyramid. (Data obtained at 10 K from NPD.)

bility ( $q_S$ ) of the spiral and the spiral transition temperature  $T_S$ , as predicted by the model of Scaramucci and co-workers [25,28] when the changes in the modulation ( $q_S$ ) are driven by raising Fe/Cu disorder. Remember that here Fe/Cu disorder is invariant and, therefore, the fraction of improper Fe/Fe bonds ( $Fe_2O_9$  bipyramids with strongly AFM Fe-O-Fe bonds) is kept constant. A central result here is that the evolution shown in Fig. 8(c) is not driven by chemical disorder, being instead fostered by the reduction of the mean elongation in the nominal  $CuO_5$  pyramids.

Recapitulating, we have shown that, besides the huge tuning of the spiral transition temperature and in parallel to the stability gain, the rotation plane of the helix is reoriented by the Cu/Co substitution, in such a way that nearby the triple point (when  $T_S$  is maximal) the spiral order adopts an almost complete cycloidal magnetic configuration.

#### IV. CONCLUSIONS

To summarize, we have demonstrated the existence of an alternative method to cation disorder that enables tuning and enhancing the stability, properties and performance of the unconventional spiral magnetic phase found in layered  $RBaCuFeO_5$  perovskites with  $YBaCuFeO_5$  structure. The new driving force consists of reducing the extra elongation of the square  $Cu^{2+}$  pyramids caused by the full occupancy of the  $3z^2 - r^2$  orbital in five-coordination. We have thus



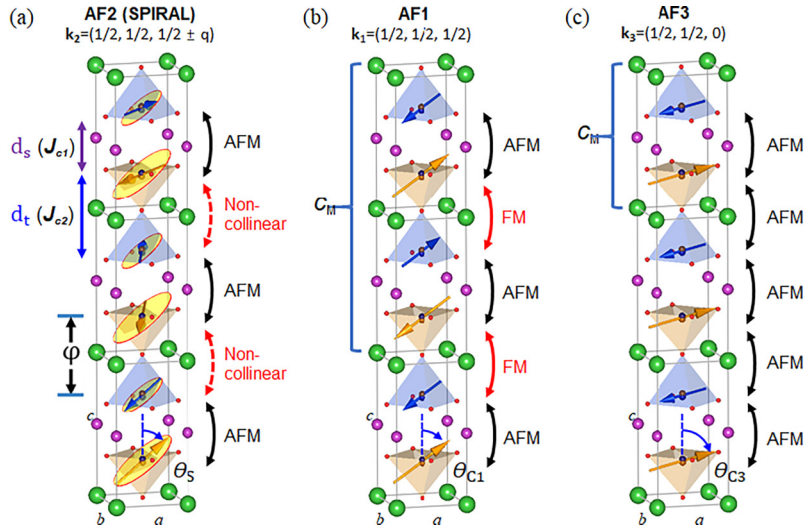


FIG. 9. Schematic projections of (a) the incommensurate spiral [AF2] and the commensurate collinear magnetic orders (b) AF1 and (c) AF3. For clarity, the average magnetic moment is depicted in each pyramid.

shown that acting on the elongated  $\text{CuO}_5$  pyramids of RBCFO perovskites opens a new avenue to push the stability of the incommensurate magnetic spirals in this singular family of compounds. Within this new approach, the stability of the spiral phase gets preserved up to temperatures over 360 K, well above room temperature, and it is achieved without modifying or increasing the Fe/Cu cation disorder in the material. Namely, the stability can be raised without altering the fraction of B antisites. This new route avoids the previously assumed obligation of applying a fast-quenching process and so generating a sufficient density of B-site antisites in the material.

The alternative avenue reported in this work opens up exciting new perspectives to be applied to the fabrication of large single crystals with magnetic spirals (and possibly multiferroic) at potentially commercial temperatures. The traveling solvent floating zone technique used to prepare YBCFO single crystals, where the very slow pulling rates favors the ordering of the different cations, entails evident difficulties to control the resulting distribution of Fe/Cu in the bipyramids. The intrinsic limitations to the growth of large crystals by floating zone methods are known to favor low fractions of Cu/Fe antisites. Very slow pulling rates favor the ordering of Cu/Fe cations and crystals without a spiral phase or too low  $T_S$  values [16,29]. It is worth remembering that if disorder ( $n_d$ ) does not exceed a critical threshold ( $n_0 \approx 0.11$  in YBCFO [12]) the insufficient magnetic frustration (deficient density of  $\text{Fe}_2\text{O}_9$  centers) cannot form a long-range incommensurate ordering. Without manipulating the Fe/Cu chemical disorder, the novel mechanism activated by divalent transition metals at the Cu sites has the ability to renormalize the fundamental exchange couplings parallel to the  $c$  axis. On one hand, a weakening of the  $J_{c1}$  exchange between neighbor (successive) bilayers (separated by the distance  $d_S$ ) can be anticipated. On the other hand, the rise of frustration producing the extraordinary enhancement of  $T_S$  reported here can only be convincingly ex-

plained by the renormalization of the strong Fe/Fe intralayer AF exchange coupling in  $\text{Fe}_2\text{O}_9$  bipyramids. The latter is the most relevant effect of the Cu/Co substitution at the B-site and it is triggered by the insertion of  $\text{Co}^{2+}\text{O}_5$  units of reduced height compared to  $\text{Cu}^{2+}\text{O}_5$  ones.

These results suggest a number of further surveys. For instance, the study of (i) the influence of, apart from cobalt, other divalent transition metals with nonelongated pyramidal coordination, including magnetic and nonmagnetic ones; (ii) the potential extension of the stability range of the spiral and the optimal cation disorder  $n_d$  that maximize the spiral transition temperature at the triple point ( $T_s^c$ ) by B-site doping; (iii) the tuning of the critical threshold ( $n_0$ ) when varying the amount of this type of B-site doping in the system; or (iv) the comparison with the application of uniaxial pressure over the  $c$  direction by physical methods.

## ACKNOWLEDGMENTS

We acknowledge financial support from the Spanish Ministerio de Ciencia, Innovación y Universidades (MINCIU), through Projects No. PID2021-124734OB-C22 and No. RTI2018-098537-B-C21, cofunded by ERDF from EU, and “Severo Ochoa” Programme for Centres of Excellence in R&D [FUNFUTURE (CEX2019-000917-S)]. And from the Generalitat de Catalunya (Project 2021-SGR-445). X.Z. was financially supported by China Scholarship Council (CSC) with Grant No. 201706080017. A.R.’s work was as a part of the Ph.D. program in Materials Science at Universitat Autònoma de Barcelona. We acknowledge the Institut Laue-Langevin (ILL) for provision of beam time (doi: 10.5291/ILL-DATA.CRG-2656 and 10.5291/ILL-DATA.CRG-2850). We thank ALBA synchrotron for the provision of beamtime via proposals 2021014856 [in-house], 2021035108, and 2017092471.

- [1] S.-W. Cheong and X. Xu, Magnetic chirality, *npj Quantum Mater.* **7**, 40 (2022).
- [2] E. Bousquet and A. Cano, Non-Collinear magnetism in multiferroic perovskites, *J. Phys. Condens. Matter* **28**, 123001 (2016).
- [3] S. Dong, J. M. Liu, S. W. Cheong, and Z. Ren, Multiferroic materials and magnetoelectric physics: Symmetry, entanglement, excitation, and topology, *Adv. Phys.* **64**, 519 (2015).
- [4] T. Kimura, Magnetoelectric hexaferrites, *Annu. Rev. Condens. Matter Phys.* **3**, 93 (2012).
- [5] V. Kocsis *et al.*, Magnetization-polarization cross-control near room temperature in hexaferrite single crystals, *Nat. Commun.* **10**, 1247 (2019).
- [6] Z. Wang *et al.*, Magnetoelectric effect and phase transitions in CuO in external magnetic fields, *Nat. Commun.* **7**, 10295 (2016).
- [7] N. Terada *et al.*, Room-temperature Type-II multiferroic phase induced by pressure in cupric oxide, *Phys. Rev. Lett.* **129**, 217601 (2022).
- [8] B. Kundys, A. Maignan, and C. Simon, Multiferroicity with high- $T_C$  in ceramics of the YBaCuFeO<sub>5</sub> ordered perovskite, *Appl. Phys. Lett.* **94**, 32 (2009).
- [9] M. Morin *et al.*, Incommensurate magnetic structure, Fe/Cu chemical disorder, and magnetic interactions in the high-temperature multiferroic YBaCuFeO<sub>5</sub>, *Phys. Rev. B* **91**, 064408 (2015).
- [10] M. Morin, E. Canévet, A. Raynaud, M. Bartkowiak, D. Sheptyakov, V. Ban, M. Kenzelmann, E. Pomjakushina, K. Conder, and M. Medarde, Tuning magnetic spirals beyond room temperature with chemical disorder, *Nat. Commun.* **7**, 13758 (2016).
- [11] J. Lyu, M. Morin, T. Shang, M. T. Fernández-Díaz, and M. Medarde, Weak ferromagnetism linked to the high-temperature spiral phase of YBaCuFeO<sub>5</sub>, *Phys. Rev. Res.* **4**, 023008 (2022).
- [12] A. Romaguera, X. Zhang, O. Fabelo, F. Fauth, J. Blasco, and J. L. García-Muñoz, Helimagnets by Disorder: Its role on the high-temperature magnetic spiral in the YBaCuFeO<sub>5</sub> perovskite, *Phys. Rev. Res.* **4**, 043188 (2022).
- [13] J. B. Goodenough, An interpretation of the magnetic properties of the perovskite-type mixed crystals La<sub>1-x</sub>Sr<sub>x</sub>CoO<sub>3-λ</sub>, *J. Phys. Chem. Solids* **6**, 287 (1958).
- [14] J. Kanamori, Superexchange interaction and symmetry properties of electron orbitals, *J. Phys. Chem. Solids* **10**, 87 (1959).
- [15] D. Dey, S. Nandy, T. Maitra, C. S. Yadav, and A. Taraphder, Nature of spiral state and absence of electric polarisation in Sr-doped YBaCuFeO<sub>5</sub> revealed by first-principle study, *Sci. Rep.* **8**, 1 (2018).
- [16] Y. C. Lai *et al.*, Magnetic ordering and dielectric relaxation in the double perovskite YBaCuFeO<sub>5</sub>, *J. Phys. Condens. Matter* **29**, 145801 (2017).
- [17] X. Zhang, A. Romaguera, O. Fabelo, F. Fauth, J. Herrero-Martín, and J. L. García-Muñoz, Tuning the tilting of the spiral plane by Mn doping in YBaCuFeO<sub>5</sub> multiferroic, *Acta Mater.* **206**, 116608 (2021).
- [18] T. Vogt, P. M. Woodward, P. Karen, B. A. Hunter, P. Henning, and A. R. Moodenbaugh, Low to high spin-state transition induced by charge ordering in antiferromagnetic YBaCo<sub>2</sub>O<sub>5</sub>, *Phys. Rev. Lett.* **84**, 2969 (2000).
- [19] N. Hollmann, Z. Hu, T. Willers, L. Bohatý, P. Becker, A. Tanaka, H. H. Hsieh, H. J. Lin, C. T. Chen, and L. H. Tjeng, Local symmetry and magnetic anisotropy in multiferroic MnWO<sub>4</sub> and antiferromagnetic CoWO<sub>4</sub> studied by soft x-ray absorption spectroscopy, *Phys. Rev. B* **82**, 184429 (2010).
- [20] F. Fauth, R. Boer, F. Gil-Ortiz, C. Popescu, O. Vallcorba, I. Peral, D. Fullà, J. Benach, and J. Juanhuix, The crystallography stations at the alba synchrotron, *Eur. Phys. J. Plus* **130**, 160 (2015).
- [21] P. E., and S. F. Alessandro Barla, Josep Nicolás, Daniele Cocco, Secundino Manuel Valvidares, Javier Herrero-Martín, Pierluigi Gargiani, Jairo Moldes, and Claude Ruget, Design and performance of BOREAS, the beamline for resonant x-ray absorption and scattering experiments at the ALBA synchrotron light source, *J. Synchr. Rad.* **23**, 1507 (2016).
- [22] J. Rodríguez-Carvajal, Recent advances in magnetic structure determination by neutron powder diffraction, *Phys. B* **192**, 55 (1993).
- [23] K. Momma and F. Izumi, VESTA 3 for three-dimensional visualization of crystal, volumetric and morphology data, *J. Appl. Crystallogr.* **44**, 1272 (2011).
- [24] See Supplemental Material at <http://link.aps.org/supplemental/10.1103/PhysRevResearch.6.033081> for details about refined synchrotron patterns and structural information; Magnetic refinements at 10 K and the spiral magnetic structures obtained increasing the Co content., n.d.
- [25] A. Scaramucci, H. Shinaoka, M. V. Mostovoy, M. Müller, C. Mudry, M. Troyer, and N. A. Spaldin, Multiferroic magnetic spirals induced by random magnetic exchanges, *Phys. Rev. X* **8**, 011005 (2018).
- [26] R. D. Shannon, Revised effective ionic radii and systematic studies of interatomic distances in halides and chalcogenides, *Acta Crystallogr. Sect. A* **32**, 751 (1976).
- [27] T. Shang, E. Canévet, M. Morin, D. Sheptyakov, M. Teresa Fernández-Díaz, E. Pomjakushina, M. Medarde, M. T. Fernández-Díaz, E. Pomjakushina, and M. Medarde, Design of magnetic spirals in layered perovskites: Extending the stability range far beyond room temperature, *Sci. Adv.* **4**, eaau6386 (2018).
- [28] A. Scaramucci, H. Shinaoka, M. V. Mostovoy, R. Lin, C. Mudry, and M. Müller, Spiral order from orientationally correlated random bonds in classical XY models, *Phys. Rev. Res.* **2**, 013273 (2020).
- [29] A. Romaguera, X. Zhang, R. Li, O. Fabelo, and J. L. García-Muñoz, Magnetic properties of highly ordered single crystals with layered YBaCuFeO<sub>5</sub> structure, *EPJ Web Conf.* **286**, 05005 (2023).